Article

Synthetic Aperture Radar Image Change Detection Based on Principal Component Analysis and Two-Level Clustering

Liangliang Li [1] , **Hongbing Ma** [2,*] , **Xueyu Zhang** [1] , **Xiaobin Zhao** [1] , **Ming Lv** [3] **and Zhenhong Jia** [3]

1   School of Information and Electronics, Beijing Institute of Technology, Beijing 100081, China
2   Department of Electronic Engineering, Tsinghua University, Beijing 100084, China
3   School of Computer Science and Technology, Xinjiang University, Urumqi 830046, China
*   Correspondence: hbma@tsinghua.edu.cn

Abstract: Synthetic aperture radar (SAR) change detection provides a powerful tool for continuous, reliable, and objective observation of the Earth, supporting a wide range of applications that require regular monitoring and assessment of changes in the natural and built environment. In this paper, we introduce a novel SAR image change detection method based on principal component analysis and two-level clustering. First, two difference images of the log-ratio and mean-ratio operators are computed, then the principal component analysis fusion model is used to fuse the two difference images, and a new difference image is generated. To incorporate contextual information during the feature extraction phase, Gabor wavelets are used to obtain the representation of the difference image across multiple scales and orientations. The maximum magnitude across all orientations at each scale is then concatenated to form the Gabor feature vector. Following this, a cascading clustering algorithm is developed within this discriminative feature space by merging the first-level fuzzy c-means clustering with the second-level neighbor rule. Ultimately, the two-level combination of the changed and unchanged results produces the final change map. Five SAR datasets are used for the experiment, and the results show that our algorithm has significant advantages in SAR change detection.

Keywords: SAR; change detection; principal component analysis; Gabor wavelets; two-level clustering

1. Introduction

Remote sensing change detection is a method that compares various images or datasets collected from the same geographic area at different times to identify and analyze changes [1,2]. This approach is widely applied across numerous sectors, including environmental monitoring, urban planning, agriculture, and disaster management [3,4]. It plays a crucial role in understanding and responding to changes in our environment and infrastructure, providing valuable insights for decision-making and policy development.

Remote sensing change detection is divided into two main types: heterogeneous and homogeneous [5]. Heterogeneous change detection focuses on comparing different types of images, such as optical remote sensing images and synthetic aperture radar (SAR) images. This area has seen significant contributions, such as Du et al. [6], who introduced a concatenated deep-learning framework for multitask change detection, combining optical and SAR images. Liu et al. [7] presented a novel approach using domain-adaptive cross reconstruction for change detection in heterogeneous remote sensing images, leveraging a feedback guidance mechanism. Xiao et al. [8] introduced a method called change alignment-based graph structure learning (CAGSL) for unsupervised heterogeneous change detection by assessing structural differences both forward and backward. Sun et al. [9,10] have contributed twice in this field, first by developing graphs based on similarity and dissimilarity relationships for multimodal change detection, and later by enhancing a nonlocal patch-based graph with a convolutional wavelet neural network (CWNN) or principal component

analysis network (PCANet), specifically for detecting changes in optical remote sensing and SAR images. Since deep-learning algorithms require training, deep-learning-based change detection algorithms are relatively time consuming. These advancements reflect the dynamic evolution of methodologies in detecting changes across heterogeneous remote sensing data.

The field of homogeneous change detection has seen significant advancements with the application of deep-learning techniques. These innovations have led to more sophisticated and efficient methods for analyzing changes in both optical remote sensing images and hyperspectral images, as well as SAR images [11–23]. For instance, Wu et al. [14] proposed a spatial–temporal association-enhanced mobile-friendly vision transformer specifically designed for the change detection of high-resolution images. This method stands out for its lightweight design and high efficiency. Similarly, Song et al. [15] introduced a network that leverages context spatial awareness for remote sensing image change detection, which relies on the graph and convolution interaction. Wang et al. [16] contributed by introducing a knowledge distillation-based lightweight change detection method for high-resolution remote sensing imagery, aimed at facilitating on-board processing. Qu et al. [17] developed a cycle-refined multidecision joint alignment network, tailored for unsupervised domain adaptive hyperspectral change detection, highlighting the continuous refinement in the field. Zhang et al. [18] presented a novel approach combining a convolution and attention mixer specifically for SAR image change detection, showcasing the ongoing evolution of methodologies. Su et al. [19] developed an unsupervised method utilizing a variational graph auto-encoder network for object-based small area change detection in SAR images, which offers benefits in reducing the adverse effects of class imbalance and suppressing speckle noise. Zhang et al. [20] introduced a robust unsupervised method for small area change detection from SAR imagery, employing a convolutional wavelet neural network, further emphasizing the field's progression towards addressing specific challenges in SAR image analysis.

Despite the impressive strides made by deep learning in the realm of SAR change detection, traditional algorithms continue to play a vital role, showcasing their enduring strengths. These traditional methods primarily involve steps such as image registration, image preprocessing (for instance, speckle noise reduction), computation of difference images (DIs), and the application of thresholds or classification techniques to produce change detection maps [21]. Notably, operators like the log-ratio (LR), mean-ratio (MR), and neighbor-ratio (NR) are extensively utilized to generate difference images [22], while methods such as the Otsu algorithm, fuzzy C-means clustering (FCM), and fuzzy local information C-means clustering are employed to derive the change maps [23]. Zhuang et al. [24] introduced a novel approach called the ratio-based nonlocal information for change detection in multitemporal SAR images. This method leverages spatial–temporal nonlocal neighborhoods, where the similarity between two pixels in the nonlocal neighborhood is effectively characterized by a ratio-based Gaussian kernel function. This technique is particularly good at retaining edge information in the change region while minimizing the overall error in the change detection results. Furthermore, Zhuang et al. [25] proposed an adaptive generalized likelihood ratio test for SAR image change detection, which excels in mitigating noise interference, preserving edge details, and enhancing the accuracy of change detection outcomes. Additionally, Gao et al. [26] developed a superpixel-based multiobjective change detection method that utilizes a self-adaptive neighborhood-based binary differential evolution algorithm, marking further advancement in traditional change detection techniques.

In this study, we introduce a SAR change detection technique that leverages principal component analysis (PCA) and two-level clustering. Our motivation is to compute a difference image that adequately reflects the changing areas, and then use classification algorithms to obtain precise detection results. This method begins by utilizing the log-ratio and mean-ratio operations to create two distinct difference images. The background in the log-ratio image appears relatively uniform, while the change-area information in the

mean-ratio image aligns closely with the actual trends observed in the remote sensing imagery. Consequently, both the log-ratio and mean-ratio images can be merged into a single, new difference image that encapsulates complementary information. Following this, a PCA fusion model merges two difference images into a single one. Subsequently, the Gabor wavelets and FCM are applied to generate the final change map.

2. The Proposed Method

In this section, we outline the proposed method for SAR image change detection, which is organized into three main steps: difference image analysis, Gabor feature extraction, and two-level clustering. This method's structure is visualized in Figure 1, showcasing the systematic approach of our change detection methodology. Further details are provided below.
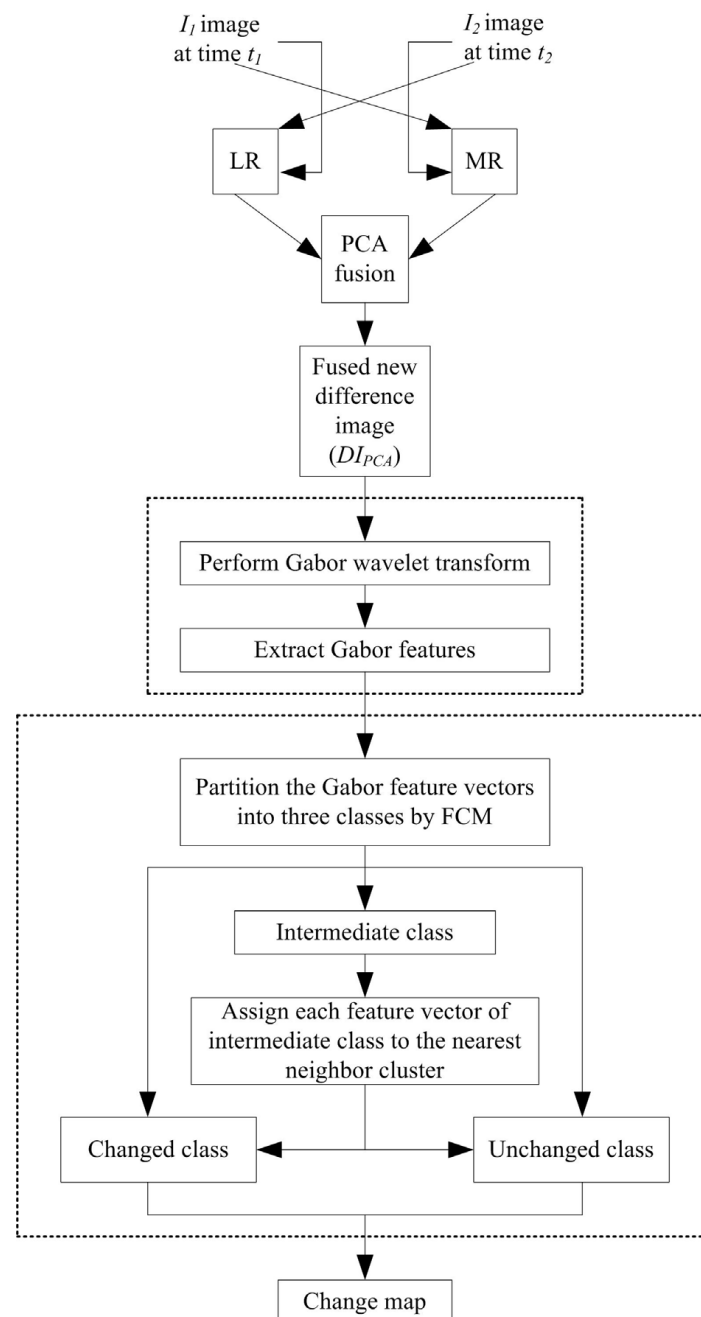
Figure 1. The structure of the proposed change detection method.

2.1. Difference Image Analysis

For two co-registered SAR images I_1 and I_2 captured at different times t_1 and t_2 over the same geographic area, the task of change detection aims to precisely identify the locations of changes between the pair of acquired images.

The difference images (DIs) of LR and MR operators are defined as follows [27]:

$$\text{DI}_{\text{LR}} = \log \frac{I_1}{I_2} \tag{1}$$

$$\text{DI}_{\text{MR}} = \begin{cases} 1 - \min\left(\frac{\alpha_2}{\alpha_1}, \frac{\alpha_1}{\alpha_2}\right), & \text{if } \alpha_2 > \alpha_1 \\ \min\left(\frac{\alpha_2}{\alpha_1}, \frac{\alpha_1}{\alpha_2}\right) - 1, & \text{if } \alpha_2 \leq \alpha_1 \end{cases} \tag{2}$$

where α_1 and α_2 represent the local mean values of image I_1 and I_2, respectively.

PCA calculates eigenvectors and eigenvalues on a global scale, concentrating the pixel energy into a smaller subset of the PCA dataset. Suppose x_i and x_j are two images to be fused, represented as column vectors [28]:

$$x_i = \begin{bmatrix} x_1 \\ x_2 \\ \vdots \\ x_N \end{bmatrix} \tag{3}$$

$$x_j = \begin{bmatrix} x_1 \\ x_2 \\ \vdots \\ x_N \end{bmatrix} \tag{4}$$

where N indicates the number of pixels.

The covariance matrix between the two source images is given by

$$Cov(x_i, x_j) = E\left[(x_i - \beta_i)(x_j - \beta_j)\right] \tag{5}$$

where the mean of all pixels is defined by

$$\beta_i = \left(\frac{1}{N}\right) \sum x_i \tag{6}$$

$$\beta_j = \left(\frac{1}{N}\right) \sum x_j \tag{7}$$

A diagonal matrix D of eigenvalues and a full matrix V, whose columns are the corresponding eigenvectors, are computed. The eigenvalues and eigenvectors are sorted in descending order, and the first 2×2 values from V and D matrices are selected for fusion. The normalized components m_1 and m_2 are derived from V based on the following conditions, and should be less than one. The V matrix contains eigenvectors, while the D matrix is a diagonal matrix that contains eigenvalues.

If $D(1,1) > D(2,2)$

where check if the first eigenvalue in the eigenvalue matrix D is greater than the second eigenvalue. Based on the magnitude of the eigenvalues, the corresponding eigenvector ($V(:,1)$ or $V(:,2)$) is selected. Each element of the chosen eigenvector is then divided by the sum of all elements in that vector. This process, commonly used for normalization, ensures the vector sums to one, facilitating further analysis or use as weights:

$$m_1 = \frac{V(1,\ 1)}{V(1,\ 1) + V(2,\ 1)} \tag{8}$$

$$m_2 = \frac{V(2, 1)}{V(1, 1) + V(2, 1)} \tag{9}$$

else

$$m_1 = \frac{V(1, 2)}{V(1, 2) + V(2, 2)} \tag{10}$$

$$m_2 = \frac{V(2, 2)}{V(1, 2) + V(2, 2)} \tag{11}$$

Here, m_1 and m_2 serve as the weights of input images in the fusion rule, which is defined by

$$y = m_1 \times x_i + m_2 \times x_j \tag{12}$$

The weights for fusion rule, m_1 and m_2, determine the extent of information fused from each source images. In this section, we utilize the PCA fusion model to merge the difference images LR and MR, producing a new difference image DI_{PCA}. The code for PCA-based fusion is provided in the Appendix A.

2.2. Gabor Feature Extraction

The Gabor wavelets have been extensively applied to image analysis due to their biological relevance and computational properties. A 2-D Gabor wavelet kernel is formulated as the product of an elliptical Gaussian envelope and a complex plane wave, defined by the following equation [29]:

$$\psi_{\mu,\nu}(z) = \frac{\|k_{\mu,\nu}\|^2}{\sigma^2} \exp\left(-\frac{\|k_{\mu,\nu}\|^2 \|z\|^2}{2\sigma^2}\right) \times \left[\exp\left(ik_{\mu,\nu}z\right) - \exp\left(-\frac{\sigma^2}{2}\right)\right] \tag{13}$$

where μ, and ν show the orientation and scale of the Gabor kernels, respectively. The norm operator is denoted as $\|\bullet\|$, $k_{\mu,\nu} = k_\nu \exp(i\varphi_\mu)$ with $\varphi_\mu = \pi\mu/8$ and $k_\nu = k_{max}/f^\nu$, k_{max} signifies the maximum frequency and f indicates the spacing factor between kernels in the frequency domain.

The Gabor wavelet representation of the difference image is achieved by convolving Y_D with a family of Gabor kernels $\{\psi_{\mu,\nu}(z) : \mu \in \{0, \ldots, U-1\}, \nu \in \{0, \ldots, V-1\}\}$, defined as

$$O_{\mu,\nu}(z) = Y_D(z) * \psi_{u,v}(z) \tag{14}$$

Here, $z = (i, j)$ represents the pixel location, and $*$ denotes the convolution operator. $O_{\mu,\nu}(z)$ presents the convolution result corresponding to the Gabor kernel at orientation μ and scale ν. U and V refer to the total number of orientations and scales, respectively. The response of (14), i.e., $O_{\mu,\nu}(z)$, is a complex-valued quantity, having the real and imaginary parts, respectively, given by $\text{Re}(O_{\mu,v}(z))$ and $\text{Im}(O_{\mu,\nu}(z))$. Consequently, $O_{\mu,\nu}(z)$ can be expressed as:

$$O_{\mu,v}(z) = A_{\mu,\nu}(z) \exp(i\theta_{\mu,\nu}(z)) \tag{15}$$

and

$$A_{\mu,\nu}(z) = \sqrt{\text{Re}(O_{\mu,\nu}(z))^2 + \text{Im}(O_{\mu,\nu}(z))^2} \tag{16}$$

$$\theta_{\mu,\nu}(z) = \frac{\arctan(\text{Im}(O_{\mu,\nu}(z)))}{\text{Re}(O_{\mu,\nu}(z))} \tag{17}$$

The real part of a Gabor wavelet kernel is regarded as a smooth filter and its imaginary part is utilized for edge detection. The magnitude $A_{\mu,\nu}(z)$, integrating the complementary information from both $\text{Re}(O_{\mu,v}(z))$ and $\text{Im}(O_{\mu,\nu}(z))$, is often chosen as the stable and discriminative feature value. However, directly concatenating the magnitude responses

from all scales and orientations to form a feature vector results in a highly dimensional feature space. To address this issue, we focus on extracting the response with maximum magnitude across all the possible orientations from the orientation sensitivity characteristic of Gabor wavelets, i.e.,

$$q_\nu = \max_{\mu \in [0, U-1]} A_{\mu,\nu}(z) \tag{18}$$

For each pixel, and considering the scale value, the compact Gabor feature vector Q is formulated as $Q = [q_0, q_1, \ldots, q_\nu, \ldots, q_{V-1}]$. Thus, Gabor features $\chi = [Q_1, \ldots, Q_{MN}]^T$ are efficiently extracted for the difference image.

2.3. Two-Level Clustering

Once the Gabor features are extracted, any clustering technique can be employed to separate the difference image into two distinct groups. However, to effectively distinguish the changed from the unchanged classes, it is crucial to choose an efficient clustering algorithm that ensures greater within-class compactness and between-class separation. To address this challenge, a two-level clustering approach is introduced in this subsection.

Its tree topology is depicted in Figure 2. Specifically, it starts from the root of the tree standing for a unique class including all the samples. In the first level, because of its simplicity and applicability, the FCM is used to divide the root node into three child nodes, respectively, representing the changed, unchanged, and intermediate classes (i.e., ω_c^1, ω_u^1, and ω_i), respectively. Pixels classified into ω_c^1 and ω_u^1 exhibit a high likelihood of being changed and unchanged. In the second level, the internal node ω_i is further divided into two leaves ω_c^2 and ω_u^2 using the nearest neighbor rule by comparing the distances of the corresponding Gabor feature vectors to the centroids of ω_c^1 and ω_u^1. Ultimately, we integrate two-level subclusters to construct the change map.
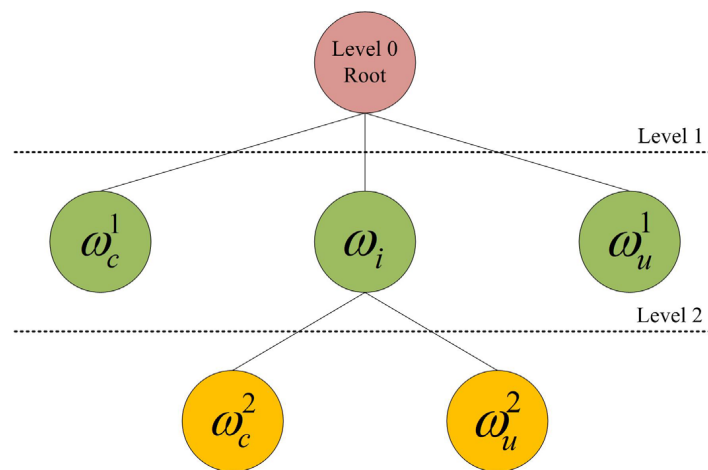
Figure 2. Tree topology of the proposed two-level clustering for change detection.

Here is an enhanced version of the description for the proposed cascade clustering approach:

Step 1. Input: given the Gabor features χ corresponding to difference image DI_{PCA} containing $M \times N$ pixels.

Step 2. Level 1: perform the FCM model on χ to partition DI_{PCA} into c clusters by minimizing the objective function:

$$J_m(u, v) = \sum_{i=1}^{c} \sum_{j=1}^{MN} u_{ij}^m \|\mathbf{x}_j - v_i\|^2 \tag{19}$$

$$\text{s.t. } u_{ij} \in [0, 1], \sum_{i=1}^{c} u_{ij} = 1 \forall j$$
$$0 < \sum_{j=1}^{MN} u_{ij} < MN \forall i \tag{20}$$

where $m \in [1, +\infty]$ represents the degree of fuzziness, v_i denotes the prototype of the *i*th cluster, $u = [u_{ij}]_{c \times MN}$ is a partition matrix with u_{ij} being the membership grade of the *j*th pixel in cluster *i*, and $v = [v_1, v_2, v_3]$ is the vector of the centroid of cluster. J_m of (19) can be iteratively optimized by alternately updating u_{ij} and v_i until convergence, i.e.,

(1) Set parameters $c = 3$, $m = 2$, $t = 0$, and initialize the partition matrix $u^{(0)}$.
(2) Calculate the centroid of the *i*th cluster by using

$$v_i^{(t+1)} = \frac{\sum_{j=1}^{MN} \left(u_{ij}^{(t)} \right)^m x_j}{\sum_{j=1}^{MN} \left(u_{ij}^{(t)} \right)^m} \tag{21}$$

(3) Update the membership grade u_{ij} by using

$$u_{ij}^{(t+1)} = \frac{\left\| x_j - v_i^{(t+1)} \right\|^{-2/(m-1)}}{\sum_{r=1}^{c} \left\| x_j - v_r^{(t+1)} \right\|^{-2/(m-1)}} \tag{22}$$

(4) Set $t := t + 1$, go to (2), and continue until convergence.
(5) Assign the pixels to a class of $\{\omega_c^1, \omega_i, \omega_u^1\}$ from

$$\text{label}\left(Y_d^{l \in \Omega_p} \right) = \begin{cases} \omega_c^1, & p = \arg\max_{i=1,2,3} M_{\Omega_i} \\ \omega_u^1, & p = \arg\min_{i=1,2,3} M_{\Omega_i} \\ \omega_i, & \text{otherwise} \end{cases} \tag{23}$$

where $\Omega_{i=1,2,3}$ show three distinct clusters identified by discriminating the highest grade of membership for each pixel from *u*. M_{Ω_i} shows the average value (i.e., the mean) of Y_D in cluster Ω_i, and it is given by:

$$M_{\Omega_i} = \left(\frac{1}{|\Omega_i|} \right) \sum_{l \in \Omega_i} Y_D^l \tag{24}$$

Step 3. Level 2: recalculate the centroids of ω_c^1 and ω_u^1 by

$$v_{\omega_c^1} = \frac{\sum_{j \in \Omega_{\omega_c^1}} (u_{ij})^m X_j}{\sum_{j \in \Omega_{\omega_c^1}} (u_{ij})^m}, \quad i \to \omega_c^1 \tag{25}$$

$$v_{\omega_u^1} = \frac{\sum_{j \in \Omega_{\omega_u^1}} (u_{ij})^m X_j}{\sum_{j \in \Omega_{\omega_u^1}} (u_{ij})^m}, \quad i \to \omega_u^1 \tag{26}$$

Following this, the nearest neighbor rule is employed to further split the intermediate class ω_i into two classes, based on:

$$\text{label}\left(Y_D^{l \in \Omega_{\omega_i}} \right) = \begin{cases} \omega_c^2, & \left\| x_l - v_{\omega_c^1} \right\|^2 \leq \left\| x_l - v_{\omega_u^1} \right\|^2 \\ \omega_u^2, & \left\| x_l - v_{\omega_c^1} \right\|^2 > \left\| x_l - v_{\omega_u^1} \right\|^2 \end{cases} \tag{27}$$

Step 4. Output: the culmination of this process produces the final change map, effectively illustrating the detected changes via

$$\Omega_{\omega_c} = \Omega_{\omega_c^1} \cup \Omega_{\omega_c^2} \tag{28}$$

$$\Omega_{\omega_u} = \Omega_{\omega_u^1} \cup \Omega_{\omega_u^2} \qquad (29)$$

3. Experimental Results and Discussions

In this section, we begin by outlining the datasets and evaluation criteria utilized in our experiments, followed by a presentation of our method's performance.

3.1. Experimental Datasets and Evaluation Criteria

We evaluated the proposed change detection method using five synthetic aperture radar (SAR) datasets. Table 1 summarizes the details of these datasets, including the event, satellites they originate from, sensor type (ST), and image size. Figures 3–9 display the images from each dataset, which consist of pairs of co-registered SAR images captured before and after changes occurred, along with a reference image annotated manually based on expert knowledge.

The effectiveness of change detection methods is assessed through both qualitative and quantitative measures. For quantitative analysis, we employ metrics such as false negatives (FNs) [30], false positives (FPs) [31–34], overall error (OE) [35], percentage of correct classifications (PCCs) [36], Kappa coefficient (KC) [37–39], and F1-score [40,41]. The formulas for these metrics are provided in Table 2.

Table 1. Descriptions of used datasets.

Datasets	Event	Satellite	Sensor Type	Size
Village of Feltwell	Land cover variations	Daedalus 1268 ATM	SAR	335×470
Ottawa	Flood	Radarsat-1	SAR	290×350
San Francisco	Flood	ERS-2	SAR	256×256
Yellow River	Flood	Radarsat-2	SAR	257×289
Sulzberger Ice Shelf	Ice breakup	European Space Agency's Envisat satellite	SAR	256×256

Table 2. Evaluation criteria.

Evaluation Metrics	Meaning	Calculation Formula
FN	Unchanged pixels that are incorrectly detected as changed pixels	-
FP	Changed pixels that are incorrectly detected as unchanged pixels	-
OE	Overall error	$OE = FN + FP$
PCC	Percentage of correct classifications	$PCC = \frac{TP+TN}{TP+TN+FN+FP}$
Kappa	Kappa coefficient	$Kappa = \frac{PCC-PRE}{1-PRE}$ $PRE = \frac{(TP+FP)\cdot(TP+FN)+(FN+TN)\cdot(FP+TN)}{(TP+TN+FP+FN)^2}$
F1	F1-score	$F1 = 2 * \frac{precision*recall}{precision+recall}$ $precision = \frac{TP}{TP+FP}$ $recall = \frac{TP}{TP+FN}$

Notes: TN (True Negative): unchanged pixels that are correctly classified. TP (True Positive): changed pixels that are correctly classified.
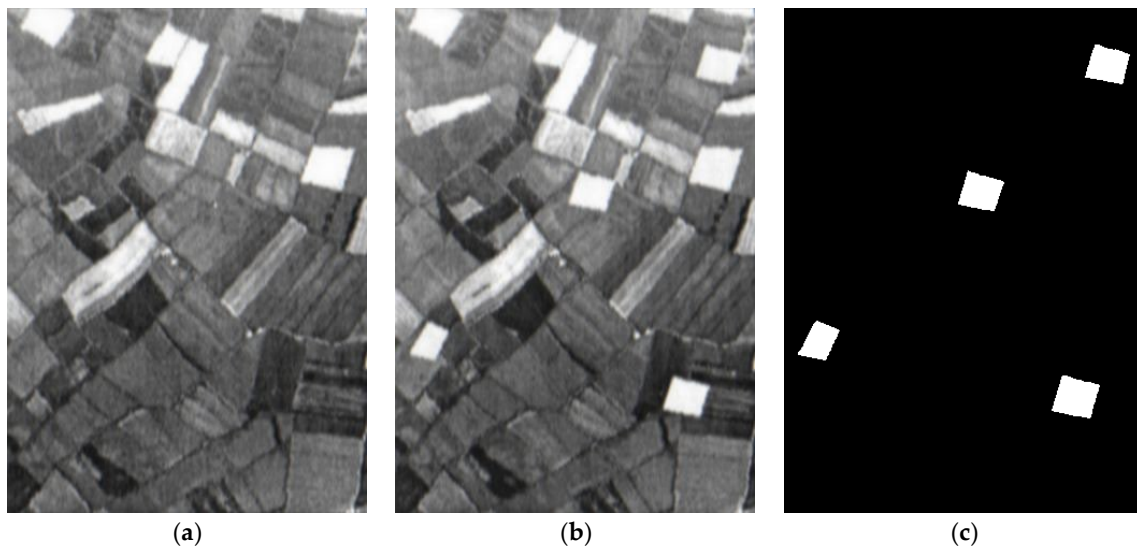
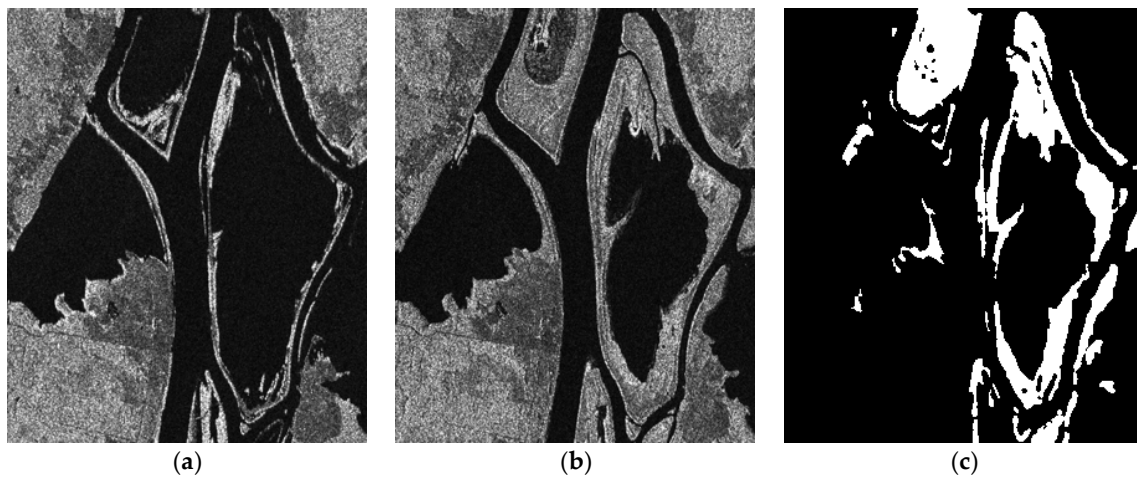**Figure 3.** Village of Feltwell dataset. (**a**) image t1; (**b**) image t2; (**c**) reference.

Figure 4. Ottawa dataset. (**a**) image acquired in May 1997; (**b**) image acquired in August 1997; (**c**) reference.
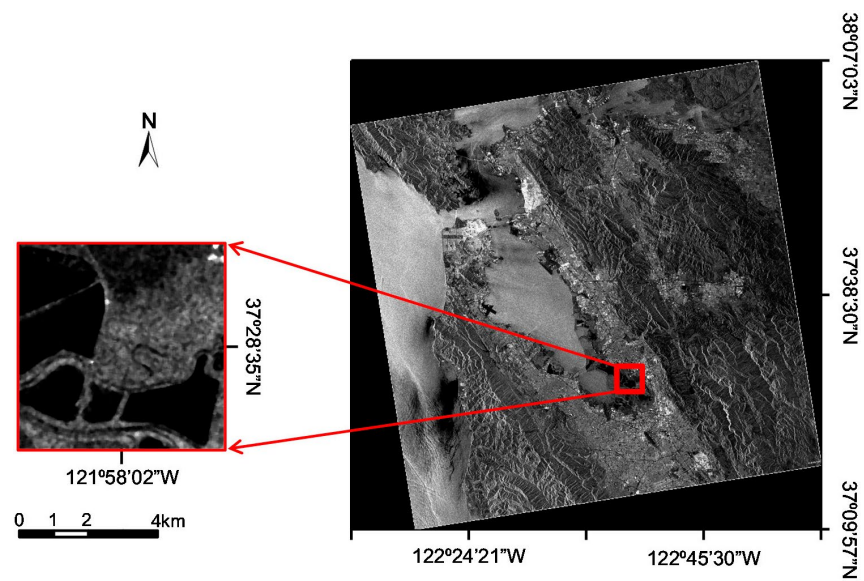

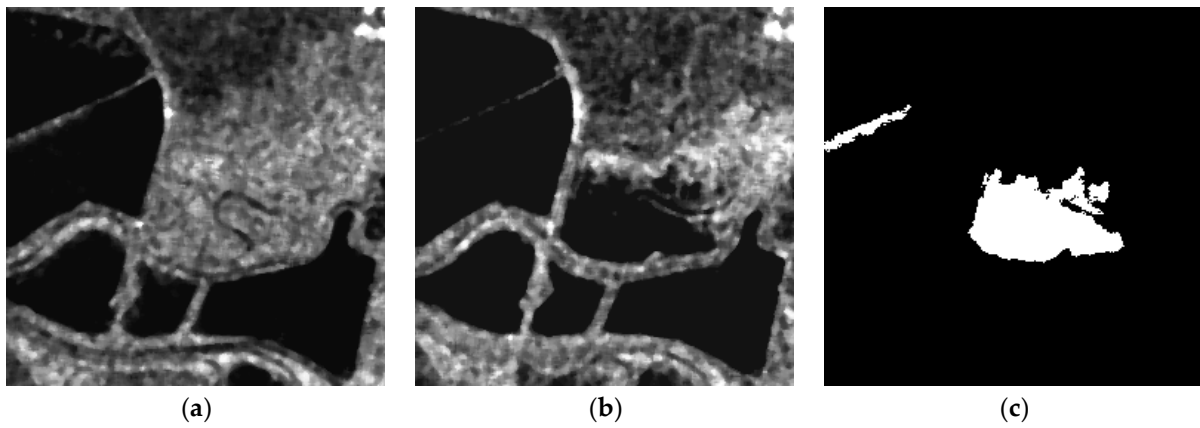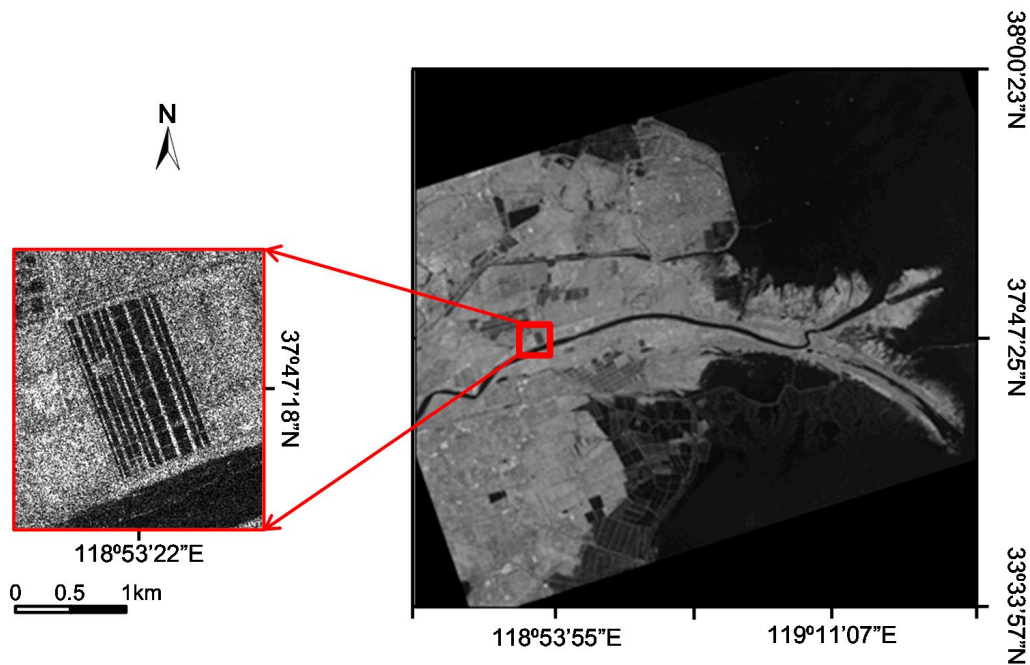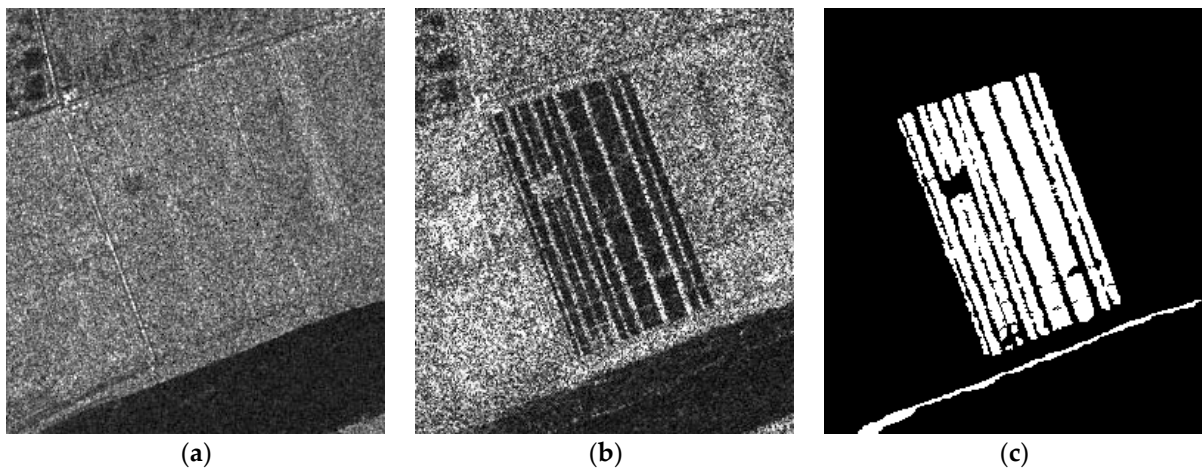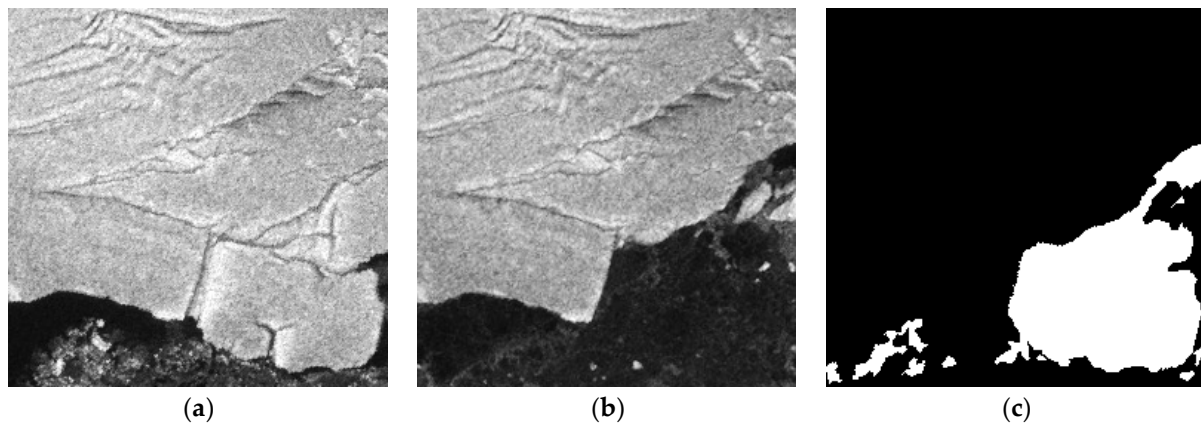**Figure 5.** SAR images acquired by ERS-2 over the city of San Francisco.

Figure 6. San Francisco dataset. (**a**) image acquired in August 2003; (**b**) image acquired in May 2004; (**c**) reference.

Figure 7. SAR images acquired by Radarsat-2 over the Yellow River Estuary in China.

**Figure 8.** Yellow River dataset. (**a**) image acquired in 2008; (**b**) image acquired in 2009; (**c**) reference.

Figure 9. Sulzberger Ice Shelf dataset. (**a**) image acquired on 11 March 2011; (**b**) image acquired on 16 March 2011; (**c**) reference.

3.2. Experimental Results and Analysis

To assess the performance of the proposed method, it was compared against seven established methods: principal component analysis and K-means (PCAKM) [42], Bayesian [43], Gabor and two-level clustering (GaborTLC) [29], logarithmic mean-based thresholding (LMT) [44], neighborhood-based ratio and collaborative representation (NRCR) [45], the adaptive generalized likelihood ratio test and maximum entropy principle for change detection in SAR images (AGLRTM) [25], and the improved nonlocal patch-based graph and principal component analysis network (INPCANet) [10]. For the parameter settings, the following are used: the $h = 3$ and $S = 9$ in the PCAKM method; in the Bayesian method, the low-pass filtering is carried out by averaging the complex values in a 5×5 sliding window; a median filter with a size of 3×3 is used in the LMT method; in the INPCANet method, $p = 2$ and neighborhood of size is 5×5; in the NRCR and AGLRTM methods, the parameters are set to the default values set by the authors of the papers, respectively; and in the proposed method and the GaborTLC method, $U = 8$, $V = 5$, $k_{\max} = 2\pi$, $f = \sqrt{2}$, and $\sigma = 2.8\pi$ are defined.

In this subsection, we examine the difference images produced by various methods and discuss the change detection outcomes achieved using the two-level clustering model. Figure 10 illustrates the difference images derived from the log-ratio operator (LR), mean-ratio operator (MR), and PCA fusion technique on the Village of Feltwell dataset, respectively.
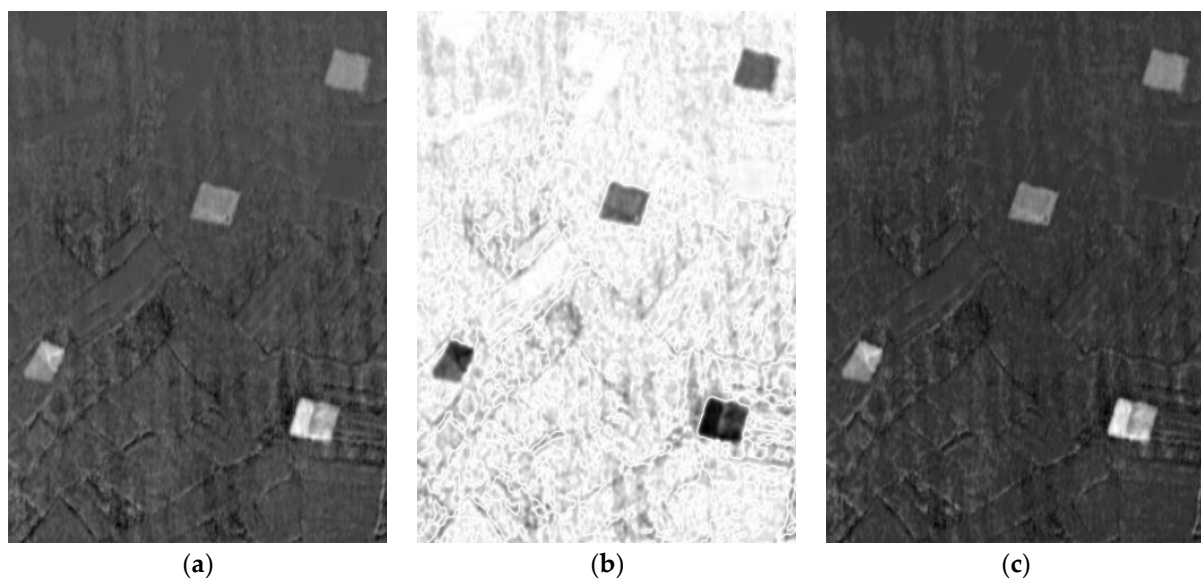
Figure 10. Difference image of Village of Feltwell dataset. (**a**) LR; (**b**) MR; (**c**) PCA.

To evaluate the efficacy of the difference images (DIs) calculated by the LR, MR, and PCA-fusion approaches, empirical receiver operating characteristic (ROC) curves are employed, as depicted in Figure 11. These curves plot the true positive rate (TPR) against the false positive rate (FPR). Additionally, two quantitative criteria based on the ROC curve—the area under the curve (AUC) and the diagonal distance (Ddist)—along with their metrics [46], are provided in Table 3. For these criteria, larger values indicate superior detection performance. According to the data in Table 3, the PCA fusion model outperforms both the LR and MR operators, showcasing its effectiveness in change detection scenarios.
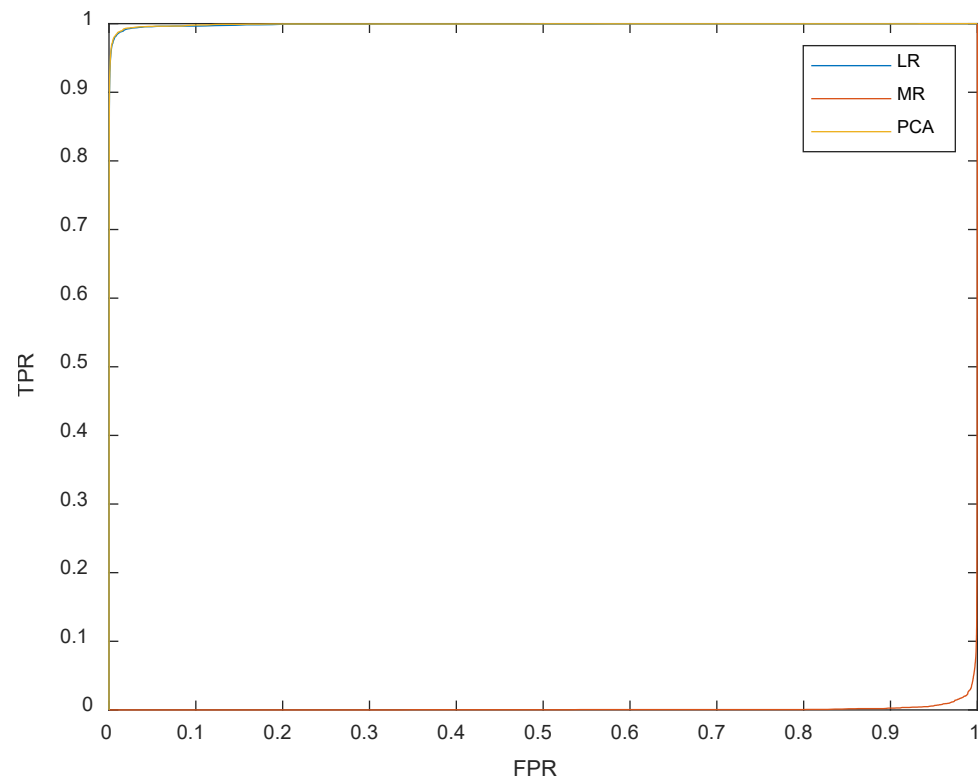

Figure 11. The ROC curves of operator-generated DIs.

Table 3. The AUC and Ddist values of different DI images on Village of Feltwell dataset.

	AUC	**Ddist**
LR	0.9986	1.3964
MR	0.0017	0.0252
PCA	0.9988	1.3977

Figure 12 presents the change detection outcomes for the Village of Feltwell dataset using the difference images processed with the two-level clustering model, with the associated performance metrics detailed in Table 4. From these visuals and data, it is observed that the log-ratio with two-level clustering (LRTLC) method exhibits the fewest false positives, with an FP value of 77. Meanwhile, the mean-ratio with two-level clustering (MRTLC) approach shows the least number of missed detections, evidenced by the FN value of 124. The PCA with two-level clustering (PCATLC) method ranks second in terms of both FN and FP, but it achieves the best performance in overall error (OE), percentage of correct classifications (PCC), Kappa coefficient (KC), and F1-score, with values of 360, 99.77%, 95.54%, and 95.66%, respectively. These results demonstrate the superior change detection capability of the fused difference image approach.
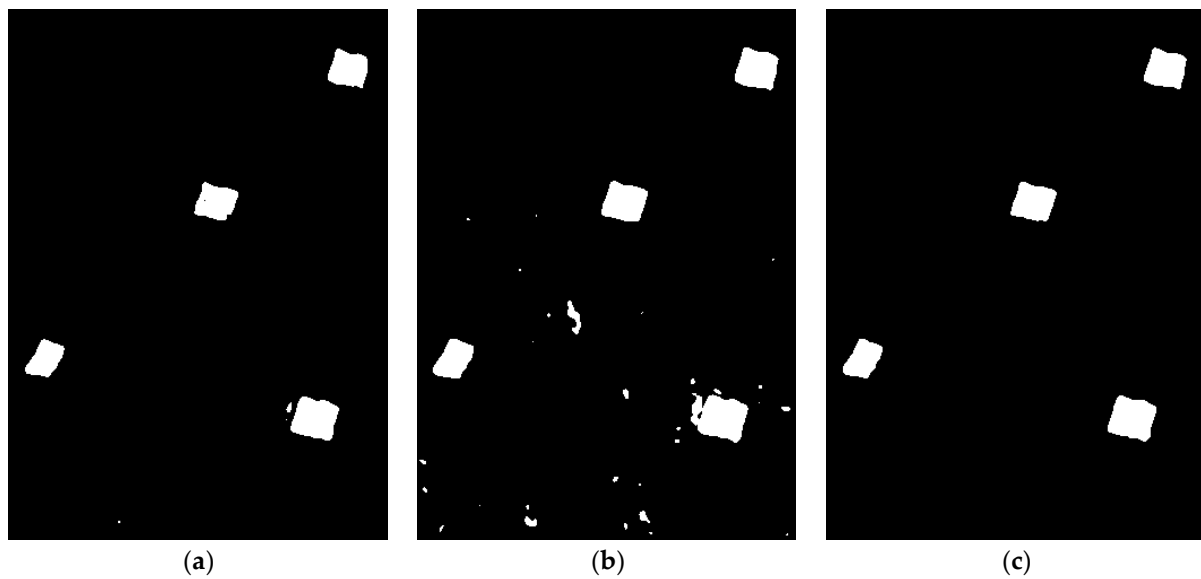
Figure 12. The change detection results of different DI images. (**a**) LRTLC; (**b**) MRTLC (**c**) PCATLC.

Table 4. The quantitative evaluation of different DI images with two-level clustering algorithm on the Village of Feltwell dataset.

	FN	FP	OE	PCC (%)	KC (%)	F1 (%)
LRTLC	539	77	616	99.61	92.11	92.31
MRTLC	124	931	1055	99.33	88.29	88.63
PCATLC	269	91	360	99.77	95.54	95.66

(1)　Results for the Village of Feltwell dataset:

The experimental outcomes for the Village of Feltwell dataset are displayed in Figure 13, with the corresponding performance metrics provided in Table 5. This figure reveals that the PCAKM, Bayesian, and LMT methods report high false positives, with values of 340, 2731, and 1863, respectively. Conversely, the NRCR, AGLRTM, and INPCANet approaches are characterized by high false negatives, with values of 1941, 2715, and 1337, respectively. The GaborTLC method has also achieved relatively good change detection effects, with the values of FN and FP being relatively balanced. Notably, the proposed method outperforms the others, showcasing the best overall performance, with an OE of 360, a PCC of 99.77%, a KC of 95.54%, an F1-score of 95.66%. The FN (269) and FP (91) both rank within the top three, respectively. These findings underscore the effectiveness of the proposed method in achieving accurate change detection.

Table 5. The quantitative evaluation of different methods for the Village of Feltwell dataset.

	FN	FP	OE	PCC (%)	KC (%)	F1 (%)
PCAKM	299	340	639	99.59	92.29	92.49
Bayesian	46	2731	2777	98.24	74.25	75.11
GaborTLC	358	177	535	99.66	93.37	93.55
LMT	127	1863	1990	98.74	79.87	80.51
NRCR	1941	14	1955	98.76	69.55	70.13
AGLRTM	2715	24	2739	98.26	51.93	52.62
INPCANet	1337	93	1430	99.09	79.77	80.22
Proposed	269	91	360	99.77	95.54	95.66
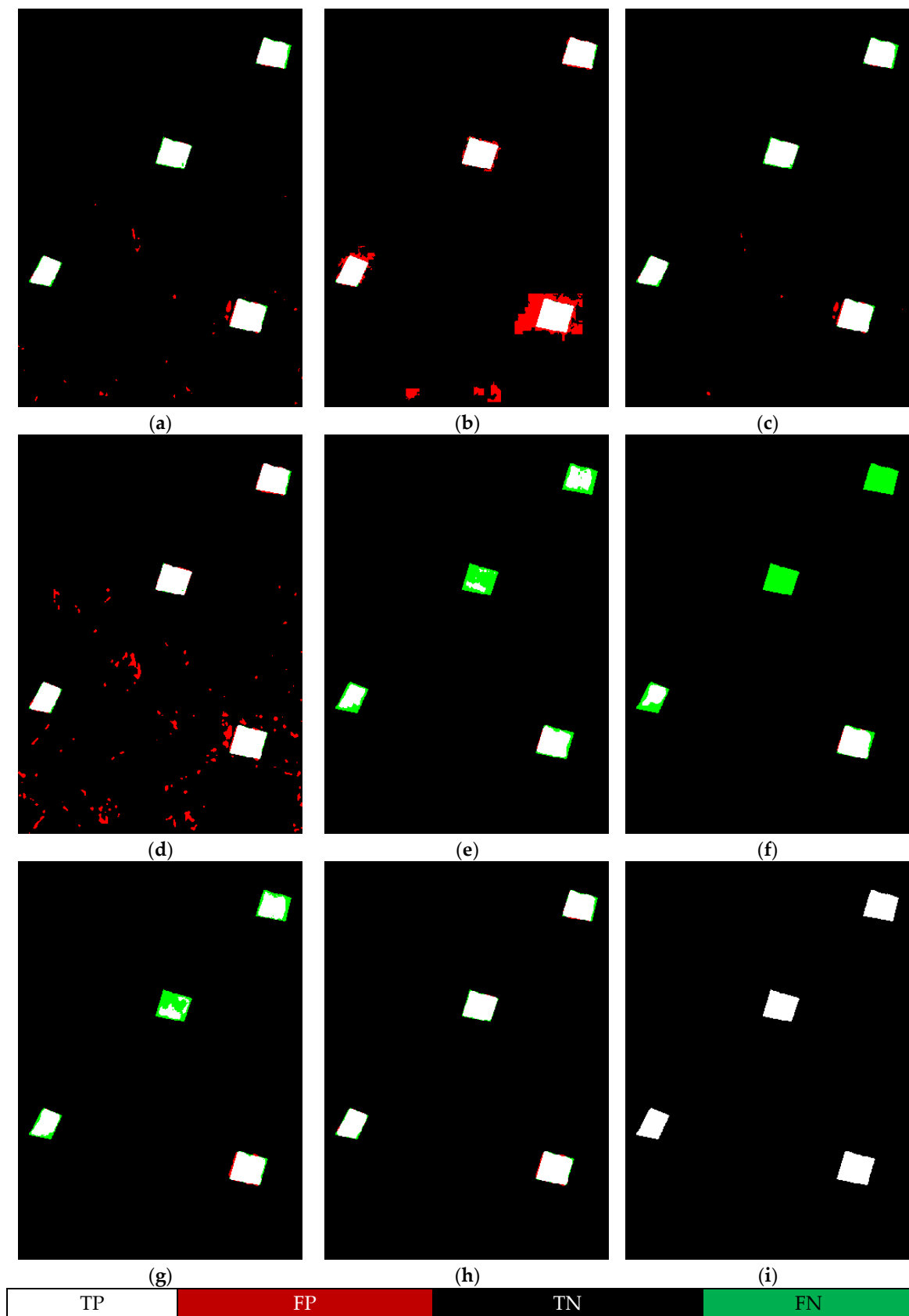
Figure 13. Results for the Village of Feltwell dataset. (**a**) PCAKM; (**b**) Bayesian; (**c**) GaborTLC; (**d**) LMT; (**e**) NRCR; (**f**) AGLRTM; (**g**) INPCANet; (**h**) proposed; (**i**) reference. In the binary change map, the following apply: white TPs; red, FPs; black, TNs; and green, FNs.
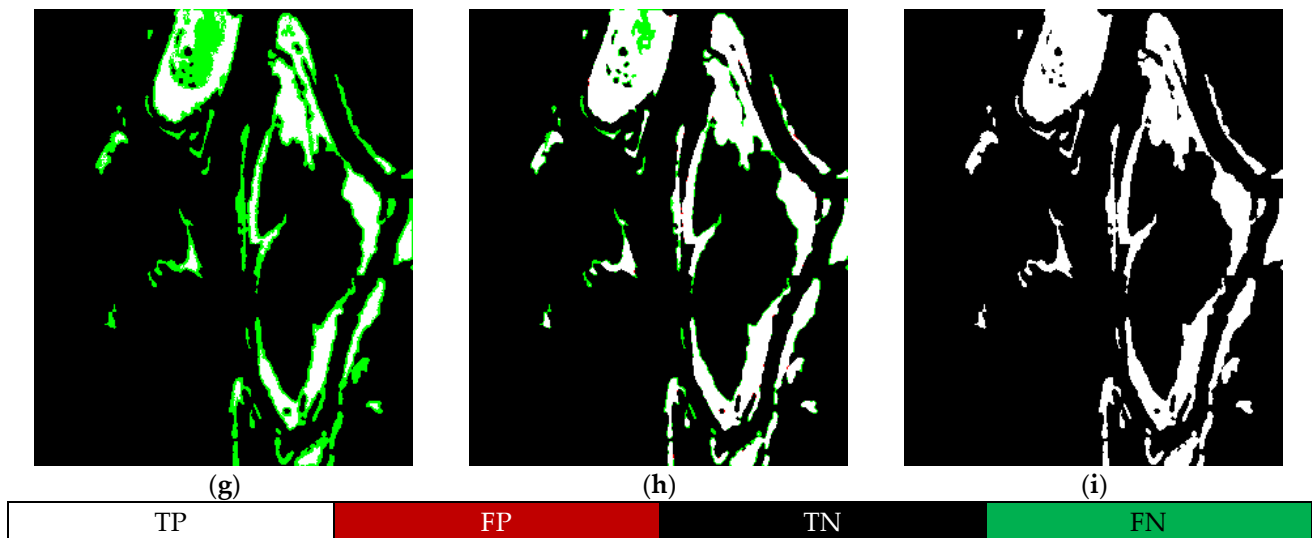
(2)   Results for the Ottawa dataset:

Figure 14 displays the experimental outcomes for the Ottawa dataset, with the related performance metrics detailed in Table 6. From this figure, it is evident that the PCAKM and Bayesian methods result in a high number of false positives, with values of 583 and 3924, respectively. Meanwhile, the LMT, NRCR, and INPCANet approaches record high false negatives, with values of 5266, 4971, and 8709, respectively. The results of the GaborTLC and AGLRTM methods are similar. It is clear from the analysis that the overall performance of the proposed method surpasses that of the comparative methods, achieving the best results in overall error (OE) of 2316, the percentage of correct classifications (PCC) of 97.72%, a Kappa coefficient (KC) of 90.92%, and an F1-score of 92.25%. Additionally, FN (2258) is one of the top three, and FP (58) is one of the top four. These results highlight the superior accuracy and reliability of the proposed method in detecting changes within the Ottawa dataset.

Table 6. The quantitative evaluation of different methods for the Ottawa dataset.

	FN	FP	OE	PCC (%)	KC (%)	F1 (%)
PCAKM	1901	583	2484	97.55	90.49	91.93
Bayesian	299	3924	4223	95.84	85.69	88.18
GaborTLC	2531	253	2784	97.26	89.07	90.66
LMT	5266	23	5289	94.79	77.43	80.31
NRCR	4971	33	5004	95.07	78.84	81.58
AGLRTM	2989	101	3090	96.96	87.66	89.42
INPCANet	8709	0	8709	91.42	58.66	62.76
Proposed	2258	58	2316	97.72	90.92	92.25

(**a**)   (**b**)   (**c**)

(**d**)   (**e**)   (**f**)

Figure 14. *Cont.*

(g)	**(h)**	**(i)**

TP	FP	TN	FN
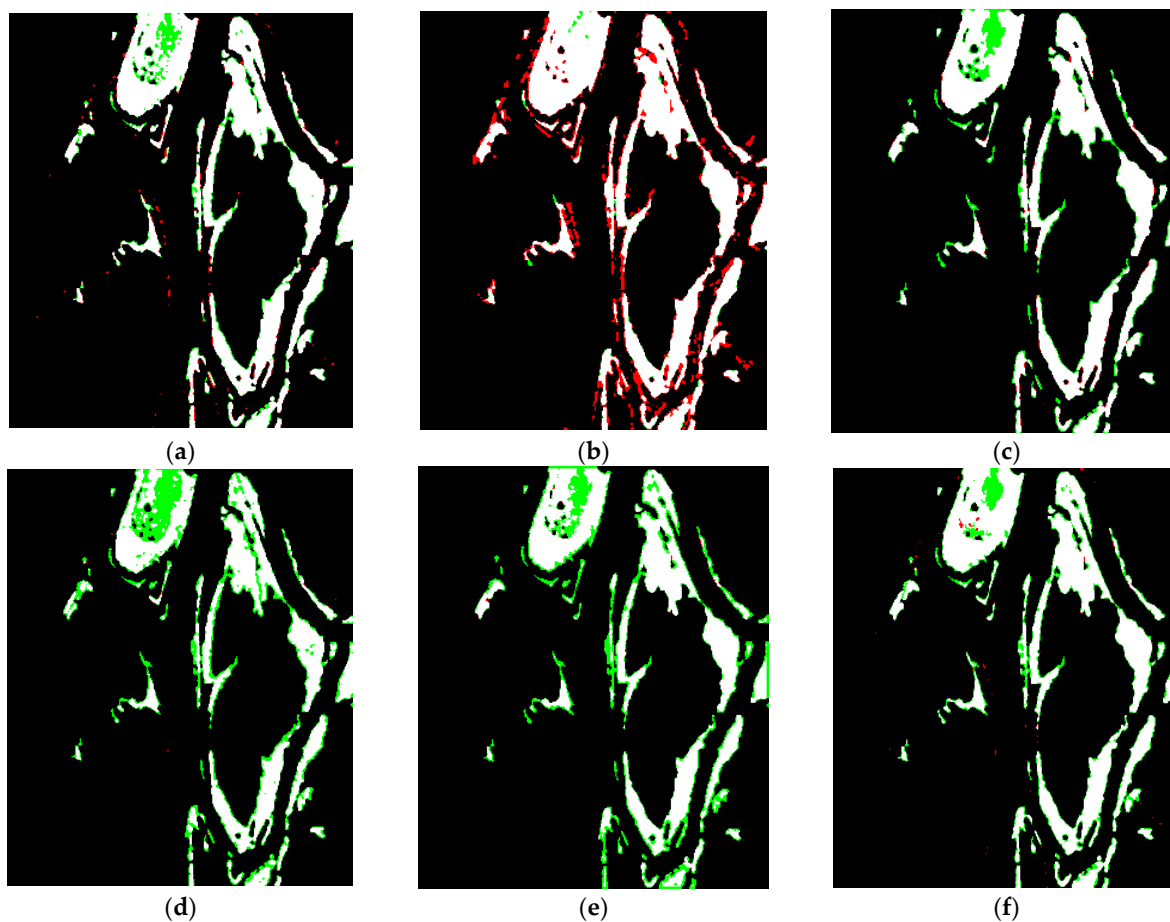
Figure 14. Results for the Ottawa dataset. (**a**) PCAKM; (**b**) Bayesian; (**c**) GaborTLC; (**d**) LMT; (**e**) NRCR; (**f**) AGLRTM; (**g**) INPCANet; (**h**) proposed; (**i**) reference.

(3) Results for the San Francisco dataset:

Figure 15 illustrates the experimental results for the San Francisco dataset, with the performance metrics detailed in Table 7. The figure highlights the fact that the PCAKM, Bayesian, GaborTLC, and AGLRTM methods exhibit high rates of false detections, with false positive (FP) values of 1023, 923, 803, and 1204, respectively. On the other hand, the LMT, NRCR, and INPCANet methods demonstrate significant rates of missed detections, with false negative (FN) values of 1046, 598, and 1120, respectively. It is apparent from the analysis that the overall performance of the proposed method outshines the comparative methods, achieving the highest scores in overall error (OE) of 840, a percentage of correct classifications (PCC) of 98.72%, a Kappa coefficient (KC) of 90.16%, and an F1-score of 90.85%. Moreover, it maintains moderate values for both FN (513) and FP (327), further evidencing its superior ability to accurately detect changes within the San Francisco dataset.

Table 7. The quantitative evaluation of different methods for the San Francisco dataset.
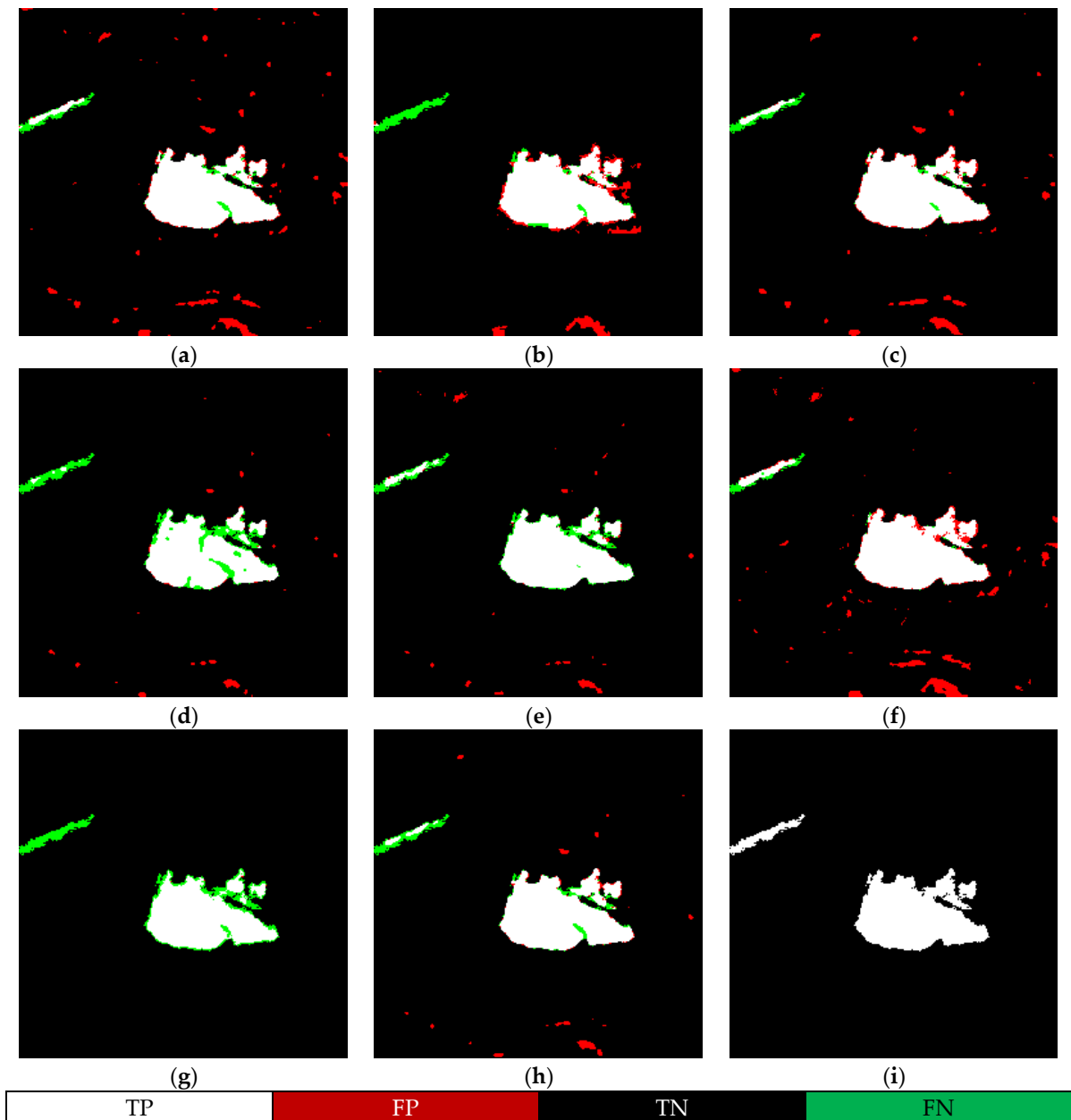
	FN	FP	OE	PCC (%)	KC (%)	F1 (%)
PCAKM	383	1023	1406	97.85	84.80	85.95
Bayesian	551	923	1474	97.75	83.66	84.87
GaborTLC	324	803	1127	98.28	87.63	88.56
LMT	1046	248	1294	98.03	83.86	84.90
NRCR	598	287	885	98.65	89.51	90.23
AGLRTM	182	1204	1386	97.89	85.53	86.66
INPCANet	1120	5	1125	98.28	85.47	86.37
Proposed	513	327	840	98.72	90.16	90.85

(4) Results for the Yellow River dataset:

Figure 16 presents the experimental outcomes for the Yellow River dataset, with performance metrics detailed in Table 8. This visualization reveals that the PCAKM, GaborTLC, NRCR, and INPCANet methods exhibit high rates of false detections, with false positive (FP) values of 4224, 1656, 2501, and 955, respectively. Conversely, the Bayesian, LMT, and AGLRTM methods show significant missed detection rates, with false negative (FN) values of 4422, 13404, and 6574, respectively. The overall performance of the proposed method stands out as the best among those evaluated, achieving the lowest overall error (OE) of 3635, the highest percentage of correct classifications (PCC) of 95.11%, the highest Kappa coefficient (KC) of 82.20%, and the highest F1-score of 85.09%. Additionally, it

maintains moderate levels for both FN (3061) and FP (574), highlighting its effective balance in accurately detecting changes within the Yellow River dataset.

TP	FP	TN	FN

Figure 15. Results for the San Francisco dataset. (**a**) PCAKM; (**b**) Bayesian; (**c**) GaborTLC; (**d**) LMT; (**e**) NRCR; (**f**) AGLRTM; (**g**) INPCANet; (**h**) proposed; (**i**) reference.

Table 8. The quantitative evaluation of different methods for the Yellow River dataset.

	FN	FP	OE	PCC (%)	KC (%)	F1 (%)
PCAKM	3359	4224	7583	89.79	66.38	72.65
Bayesian	4422	535	4957	93.33	74.61	78.43
GaborTLC	2869	1656	4525	93.91	78.69	82.36
LMT	13404	0	13404	81.95	0.34	0.42
NRCR	2256	2501	4757	93.60	78.54	82.45
AGLRTM	6574	192	6766	90.89	62.27	66.97
INPCANet	2788	955	3743	94.96	82.04	85.05
Proposed	3061	574	3635	95.11	82.20	85.09
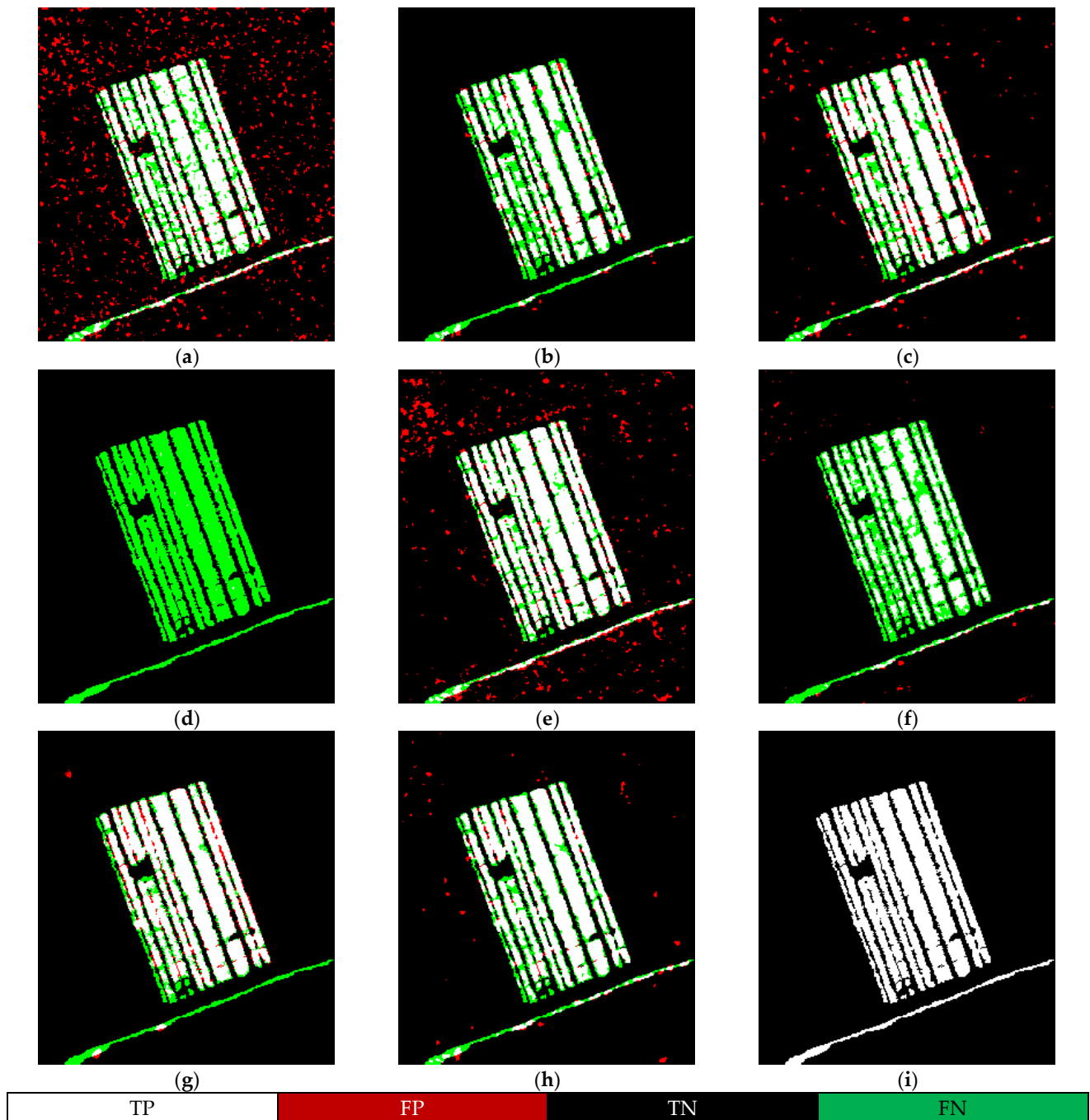
Figure 16. Results for the Yellow River dataset. (**a**) PCAKM; (**b**) Bayesian; (**c**) GaborTLC; (**d**) LMT; (**e**) NRCR; (**f**) AGLRTM; (**g**) INPCANet; (**h**) proposed; (**i**) reference.

(5)   Results for the Sulzberger Ice Shelf dataset:

Figure 17 displays the experimental results for the Sulzberger Ice Shelf dataset, with performance metrics outlined in Table 9. This visual representation shows that the PCAKM, Bayesian, and INPCANet methods have considerable false detection issues, with false positive (FP) values of 733, 7734, and 1621, respectively. On the other hand, the LMT, NRCR, AGLRTM, and INPCANet methods exhibit notable missed detection issues, with false negative (FN) values of 5322, 466, 1173, and 2330, respectively. The GaborTLC method excels, achieving the lowest overall error (OE) of 512, the highest percentage of correct classifications (PCC) of 99.22%, the highest Kappa coefficient (KC) of 97.48%, and the highest F1-score of 97.96%. Our proposed algorithm is ranked second in overall change

detection performance, with metrics of OE (747), PCC (98.86%), KC (96.34%), and F1-score (97.05%), which underscores the robustness of our approach in detecting changes.
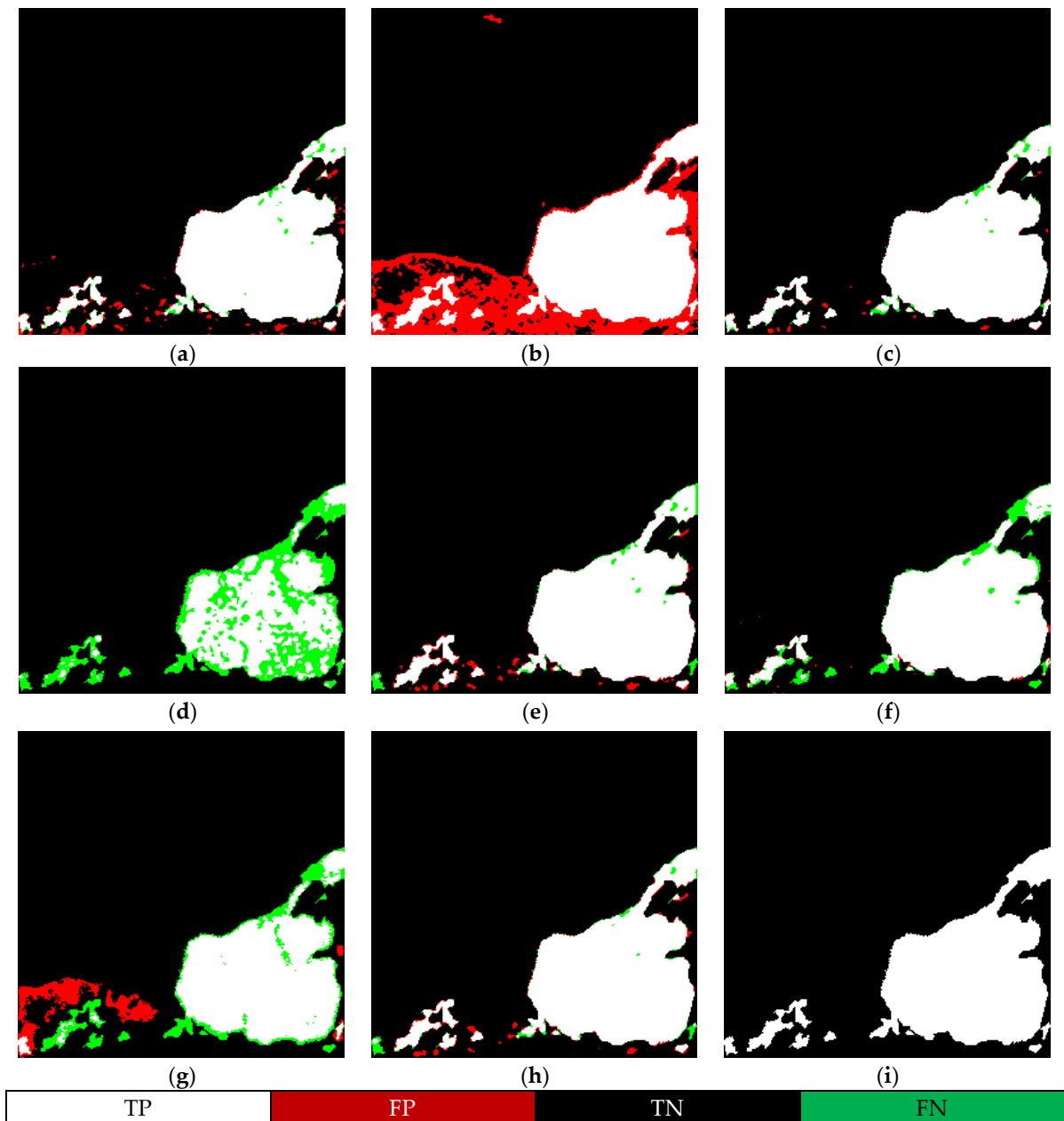
Figure 17. Results for the Sulzberger Ice Shelf dataset. (**a**) PCAKM; (**b**) Bayesian; (**c**) GaborTLC; (**d**) LMT; (**e**) NRCR; (**f**) AGLRTM; (**g**) INPCANet; (**h**) proposed; (**i**) reference.

Table 9. The quantitative evaluation of different methods for the Sulzberger Ice Shelf dataset.

	FN	**FP**	**OE**	**PCC**	**KC**	**F1**
PCAKM	322	733	1055	98.39	94.88	95.88
Bayesian	0	7734	7734	88.20	69.22	76.53
GaborTLC	307	205	512	99.22	97.48	97.96
LMT	5322	1	5323	91.88	68.86	73.25
NRCR	466	527	993	98.48	95.13	96.07
AGLRTM	1173	128	1301	98.01	93.40	94.62
INPCANet	2330	1621	3951	93.97	80.18	83.88
Proposed	338	409	747	98.86	96.34	97.05

3.3. Discussion

Based on the aforementioned results, we can summarize the performance of the proposed change detection method as follows: the proposed method was rigorously evaluated across five distinct SAR datasets: Village of Feltwell, Ottawa, San Francisco, Yellow River, and Sulzberger Ice Shelf, demonstrating its robustness and effectiveness in detecting changes. For the Yellow River dataset, although the range of variation in this dataset is relatively regular, the presence of significant noise and multiple targets results in comparatively low detection accuracy. By employing a combination of Gabor feature extraction and the two-level clustering model, including the fuzzy C-means (FCM) algorithm and PCA fusion, this method outperformed several established approaches such as PCAKM, Bayesian, GaborTLC, LMT, NRCR, AGLRTM, and INPCANet in various metrics.

The proposed method consistently achieved high performance metrics across all datasets, with notable scores in the overall error (OE), percentage of correct classifications (PCC), Kappa coefficient (KC), and F1-score, indicating a superior ability to accurately detect both changes and non-changes in complex SAR imagery. False positives (FPs) and false negatives (FNs) maintained moderate levels, demonstrating the method's balanced sensitivity and specificity in identifying changed and unchanged areas, respectively. The PCA fusion model, in particular, was highlighted for its effectiveness in enhancing change detection performance by leveraging the complementary strengths of the log-ratio and mean-ratio operators. In our subsequent work, we will attempt to use algorithms such as edge-preserving filtering [47], contourlet [48], shearlet [49–51], etc., for processing LR and MR fusion.

These results underscore the proposed method's advanced capability in SAR image change detection, combining effective feature extraction with sophisticated clustering techniques to deliver accurate and reliable change maps. This method stands as a significant contribution to the field of remote sensing, especially for applications requiring precise monitoring and analysis of environmental changes, urban development, and disaster assessment.

4. Conclusions

In this study, we propose an innovative method for change detection in SAR imagery, leveraging PCA and a two-level clustering approach. Initially, we compute two distinct difference images utilizing the log-ratio and mean-ratio techniques. Following this, a PCA fusion model is employed to amalgamate these difference images, producing a new, composite difference image. To integrate contextual information within the feature extraction phase, we utilize Gabor wavelets. This approach enables the representation of the difference image across multiple scales and orientations. For each scale, we select the maximum magnitude across all orientations to compile a Gabor feature vector. Subsequently, we develop a cascade clustering algorithm within this discriminative feature space, seamlessly integrating a first-level FCM with a second-level neighbor rule for enhanced precision. This two-tiered approach effectively segregates the changed from the unchanged areas, culminating in the creation of the definitive change map. Our methodology is rigorously tested across five SAR datasets, with the outcomes affirming its efficacy and robustness in change detection applications.

Author Contributions: The experimental measurements and data collection were carried out by L.L., H.M., X.Z. (Xueyu Zhang), X.Z. (Xiaobin Zhao), M.L. and Z.J. The manuscript was written by L.L. with the assistance of H.M., X.Z. (Xueyu Zhang), X.Z. (Xiaobin Zhao), M.L. and Z.J. All authors have read and agreed to the published version of the manuscript.

Institutional Review Board Statement: Not applicable.

Informed Consent Statement: Not applicable.

Data Availability Statement: Not applicable.

Conflicts of Interest: The authors declare no conflicts of interest.

Appendix A

```
function Y = fuse_pca(M1, M2)
%Y = fuse_pca(M1, M2) image fusion with PCA method
%      M1—input image #1
%      M2—input image #2
%      Y—fused image
% check inputs
[z1 s1] = size(M1);
[z2 s2] = size(M2);
if (z1 ~= z2) | (s1 ~= s2)
   error('Input images are not of same size');
end;
% compute, select and normalize eigenvalues
[V, D] = eig(cov([M1(:) M2(:)]));
if (D(1,1) > D(2,2))
   a = V(:,1)./sum(V(:,1));
else
   a = V(:,2)./sum(V(:,2));
end;
% fuse
Y = a(1)*M1+a(2)*M2;
```

References

1. Tang, Y.; Yang, X.; Han, T.; Zhang, F.; Zou, B.; Feng, H. Enhanced graph structure representation for unsupervised heterogeneous change detection. *Remote Sens.* **2024**, *16*, 721. [CrossRef]
2. Zhuang, H.; Fan, H.; Deng, K.; Yao, G. A Spatial-temporal adaptive neighborhood-based ratio approach for change detection in SAR images. *Remote Sens.* **2018**, *10*, 1295. [CrossRef]
3. Li, L.; Ma, H.; Jia, Z. Change detection from SAR images based on convolutional neural networks guided by saliency enhancement. *Remote Sens.* **2021**, *13*, 3697. [CrossRef]
4. Zhuang, H.; Fan, H. Change detection in SAR images based on progressive nonlocal theory. *IEEE Trans. Geosci. Remote Sens.* **2022**, *60*, 5229213. [CrossRef]
5. Lv, Z.; Liu, J.; Sun, W. Hierarchical attention feature fusion-based network for land cover change detection with homogeneous and heterogeneous remote sensing images. *IEEE Trans. Geosci. Remote Sens.* **2023**, *61*, 4411115. [CrossRef]
6. Du, Z.; Li, X.; Miao, J. Concatenated deep-learning framework for multitask change detection of optical and SAR images. *IEEE J. Sel. Top. Appl. Earth Obs. Remote Sens.* **2024**, *17*, 719–731. [CrossRef]
7. Liu, Q.; Ren, K.; Meng, X. Domain adaptive cross reconstruction for change detection of heterogeneous remote sensing images via a feedback guidance mechanism. *IEEE Trans. Geosci. Remote Sens.* **2023**, *61*, 4507216. [CrossRef]
8. Xiao, K.; Sun, Y.; Kuang, G.; Lei, L. Change alignment-based graph structure learning for unsupervised heterogeneous change detection. *IEEE Geosci. Remote Sens. Lett.* **2023**, *20*, 2504405. [CrossRef]
9. Sun, Y.; Lei, L.; Li, Z.; Kuang, G. Similarity and dissimilarity relationships based graphs for multimodal change detection. *ISPRS J. Photogramm. Remote Sens.* **2024**, *208*, 70–88. [CrossRef]
10. Sun, Y.; Lei, L.; Li, X.; Tan, X.; Kuang, G. Structure consistency-based graph for unsupervised change detection with homogeneous and heterogeneous remote sensing images. *IEEE Trans. Geosci. Remote Sens.* **2022**, *60*, 4700221. [CrossRef]
11. Chen, M.; Jiang, W.; Zhou, Y. DTT-CGINet: A dual temporal transformer network with multi-scale contour-guided graph interaction for change detection. *Remote Sens.* **2024**, *16*, 844. [CrossRef]
12. Seydi, S.T.; Boueshagh, M.; Namjoo, F.; Minouei, S.M.; Nikraftar, Z.; Amani, M. A hyperspectral change detection (HCD-Net) framework based on double stream convolutional neural networks and an attention module. *Remote Sens.* **2024**, *16*, 827. [CrossRef]
13. Li, L.; Ma, H.; Jia, Z. Multiscale geometric analysis fusion-based unsupervised change detection in remote sensing images via FLICM model. *Entropy* **2022**, *24*, 291. [CrossRef] [PubMed]
14. Wu, S.; Liu, Y.; Liu, S. Change detection enhanced by spatial-temporal association for bare soil land using remote sensing images. *IEEE J. Sel. Top. Appl. Earth Obs. Remote Sens.* **2024**, *17*, 150–161. [CrossRef]
15. Song, X.; Hua, Z.; Li, J. Context spatial awareness remote sensing image change detection network based on graph and convolution interaction. *IEEE Trans. Geosci. Remote Sens.* **2024**, *62*, 3000316. [CrossRef]

16. Wang, G.; Zhang, N.; Wang, J. Knowledge distillation-based lightweight change detection in high-resolution remote sensing imagery for on-board processing. *IEEE J. Sel. Top. Appl. Earth Obs. Remote Sens.* **2024**, *17*, 3860–3877. [CrossRef]
17. Qu, J.; Dong, W.; Yang, Y. Cycle-refined multidecision joint alignment network for unsupervised domain adaptive hyperspectral change detection. *IEEE Trans. Neural Netw. Learn. Syst.* **2024**. [CrossRef] [PubMed]
18. Zhang, H.; Li, Z.; Gao, F. Convolution and attention mixer for synthetic aperture radar image change detection. *IEEE Geosci. Remote Sens. Lett.* **2023**, *20*, 4012105. [CrossRef]
19. Su, H.; Zhang, X. Nonlocal feature learning based on a variational graph auto-encoder network for small area change detection using SAR imagery. *ISPRS J. Photogramm. Remote Sens.* **2022**, *193*, 137–149. [CrossRef]
20. Zhang, X.; Su, H. Robust unsupervised small area change detection from SAR imagery using deep learning. *ISPRS J. Photogramm. Remote Sens.* **2021**, *173*, 79–94. [CrossRef]
21. Li, L.; Ma, H.; Jia, Z. Gamma correction-based automatic unsupervised change detection in SAR images via FLICM model. *J. Indian Soc. Remote Sens.* **2023**, *51*, 1077–1088. [CrossRef]
22. Kılıç, D.K.; Nielsen, P. Comparative analyses of unsupervised PCA K-means change detection algorithm from the viewpoint of follow-up plan. *Sensors* **2022**, *22*, 9172. [CrossRef]
23. Kumar, J.; Yennapusa, M.; Rao, B. TRI-SU-L ADWT-FCM: TRI-SU-L-based change detection in SAR images with ADWT and fuzzy C-means clustering. *J. Indian Soc. Remote Sens.* **2022**, *50*, 1667–1687. [CrossRef]
24. Zhuang, H.; Hao, M. Change detection in SAR images via ratio-based gaussian kernel and nonlocal theory. *IEEE Trans. Geosci. Remote Sens.* **2022**, *60*, 5210215. [CrossRef]
25. Zhuang, H.; Tan, D. Adaptive generalized likelihood ratio test for change detection in SAR images. *IEEE Geosci. Remote Sens. Lett.* **2020**, *17*, 416–420. [CrossRef]
26. Gao, T.; Li, H.; Gong, M. Superpixel-based multiobjective change detection based on self-adaptive neighborhood-based binary differential evolution. *Expert Syst. Appl.* **2023**, *212*, 118811. [CrossRef]
27. Gong, M.; Gao, T.; Zhang, M. An M-nary SAR image change detection based on GAN architecture search. *IEEE Trans. Geosci. Remote Sens.* **2023**, *61*, 4503718. [CrossRef]
28. Vijayarajan, R.; Muttan, S. Iterative block level principal component averaging medical image fusion. *Optik* **2014**, *125*, 4751–4757. [CrossRef]
29. Li, H.; Celik, T. Gabor feature based unsupervised change detection of multitemporal SAR images based on two-level clustering. *IEEE Geosci. Remote Sens. Lett.* **2015**, *12*, 2458–2462.
30. Wang, J.; Gao, F. Change detection from synthetic aperture radar images via graph-based knowledge supplement network. *IEEE J. Sel. Top. Appl. Earth Obs. Remote Sens.* **2022**, *15*, 1823–1836. [CrossRef]
31. Gao, Y.; Gao, F. Synthetic aperture radar image change detection via siamese adaptive fusion network. *IEEE J. Sel. Top. Appl. Earth Obs. Remote Sens.* **2021**, *14*, 10748–10760. [CrossRef]
32. Zhao, X.; Liu, K.; Gao, K.; Li, W. Hyperspectral time-series target detection based on spectral perception and spatial-temporal tensor decomposition. *IEEE Trans. Geosci. Remote Sens.* **2023**, *61*, 5520812. [CrossRef]
33. Zhang, X.; Li, Q. FD-Net: Feature distillation network for oral squamous cell carcinoma lymph node segmentation in hyperspectral imagery. *IEEE J. Biomed. Health Inform.* **2024**, *28*, 1552–1563. [CrossRef] [PubMed]
34. Zhang, X.; Li, W. Hyperspectral pathology image classification using dimension-driven multi-path attention residual network. *Expert Syst. Appl.* **2023**, *230*, 120615. [CrossRef]
35. Zhang, J.; Liu, Y.; Wang, B.; Chen, C. A hierarchical fusion SAR image change-detection method based on HF-CRF model. *Remote Sens.* **2023**, *15*, 2741. [CrossRef]
36. Qu, X.; Gao, F. Change detection in synthetic aperture radar images using a dual-domain network. *IEEE Geosci. Remote Sens. Lett.* **2022**, *19*, 4013405. [CrossRef]
37. Wang, M.; Zhang, J. An adaptive and adjustable maximum-likelihood estimator for SAR change detection. *IEEE Trans. Geosci. Remote Sens.* **2022**, *60*, 5227513. [CrossRef]
38. Gao, Y.; Zhang, M.; Wang, J. Cross-scale mixing attention for multisource remote sensing data fusion and classification. *IEEE Trans. Geosci. Remote Sens.* **2023**, *61*, 5507815. [CrossRef]
39. Wang, J.; Zhao, T. A hierarchical heterogeneous graph for unsupervised SAR image change detection. *IEEE Geosci. Remote Sens. Lett.* **2022**, *19*, 4516605. [CrossRef]
40. Wang, J.; Zeng, F.; Zhang, A.; You, T. A global patch similarity-based graph for unsupervised SAR image change detection. *Remote Sens. Lett.* **2024**, *15*, 353–362. [CrossRef]
41. Murdaca, G.; Ricciuti, F.; Rucci, A.; Le Saux, B.; Fumagalli, A.; Prati, C. A semi-supervised deep learning framework for change detection in open-pit mines using SAR imagery. *Remote Sens.* **2023**, *15*, 5664. [CrossRef]
42. Celik, T. Unsupervised change detection in satellite images using principal component analysis and k-means clustering. *IEEE Geosci. Remote Sens. Lett.* **2009**, *6*, 772–776. [CrossRef]
43. Celik, T. A Bayesian approach to unsupervised multiscale change detection in synthetic aperture radar images. *Signal Process.* **2010**, *90*, 1471–1485. [CrossRef]
44. Sumaiya, M.; Kumari, R. Logarithmic mean-based thresholding for SAR image change detection. *IEEE Geosci. Remote Sens. Lett.* **2016**, *13*, 1726–1728. [CrossRef]

45. Gao, Y.; Gao, F.; Dong, J. Sea ice change detection in SAR images based on collaborative representation. In Proceedings of the IEEE International Symposium on Geoscience and Remote Sensing IGARSS, Valencia, Spain, 22–27 July 2018; pp. 7320–7323.
46. Sun, Y.; Lei, L. Image regression with structure cycle consistency for heterogeneous change detection. *IEEE Trans. Neural Netw. Learn. Syst.* **2024**, *35*, 1613–1627. [CrossRef]
47. Li, L.; Lv, M.; Jia, Z.; Jin, Q.; Liu, M.; Chen, L.; Ma, H. An effective infrared and visible image fusion approach via rolling guidance filtering and gradient saliency map. *Remote Sens.* **2023**, *15*, 2486. [CrossRef]
48. Li, L.; Ma, H.; Jia, Z.; Si, Y. A novel multiscale transform decomposition based multi-focus image fusion framework. *Multimed. Tools Appl.* **2021**, *80*, 12389–12409. [CrossRef]
49. Li, L.; Lv, M.; Jia, Z.; Ma, H. Sparse representation-based multi-focus image fusion method via local energy in shearlet domain. *Sensors* **2023**, *23*, 2888. [CrossRef] [PubMed]
50. Li, L.; Si, Y.; Wang, L.; Jia, Z.; Ma, H. A novel approach for multi-focus image fusion based on SF-PAPCNN and ISML in NSST domain. *Multimed. Tools Appl.* **2020**, *79*, 24303–24328. [CrossRef]
51. Li, L.; Ma, H. Saliency-guided nonsubsampled shearlet transform for multisource remote sensing image fusion. *Sensors* **2021**, *21*, 1756. [CrossRef]